

Nocturnal turbulence at Jezero crater, as determined from MEDA measurements and modeling

Jorge Pla-García¹, Asier Munguira², Claire Newman³, Tanguy Bertrand⁴, German Martinez⁵, Ricardo Hueso², Agustín Sánchez-Lavega⁶, Teresa del Rio-Gaztelurrutia⁷, Alexander E Stott⁸, Naomi Murdoch⁹, Manuel de la Torre Juárez¹⁰, Mark T Lemmon¹¹, Hannu Savijärvi¹², Mark Ian Richardson³, Eduardo Sebastian Martínez¹³, Alain Lepinette Malvitte¹⁴, Luis Mora Sotomayor¹³, José A Rodríguez-Manfredi¹, Daniel Viúdez-Moreiras¹⁵, Mercedes Marin¹⁵, Scot Rafkin¹⁶, and Baptiste Chide¹⁷

¹Centro de Astrobiología (CSIC-INTA)

²UPV/EHU

³Aeolis Research

⁴Paris Observatory

⁵Lunar and Planetary Institute

⁶Universidad del País Vasco UPV/EHU

⁷Universidad País Vasco UPV/EHU

⁸Institut Supérieur de l'Aéronautique et de l'Espace (ISAE-SUPAERO)

⁹ISAE SUPAERO

¹⁰Jet Propulsion Laboratory- California Institute of Technology, Pasadena, CA, USA

¹¹Space Science Institute

¹²University of Helsinki

¹³Centro de Astrobiología

¹⁴Centro de Astrobiología, INTA-CSIC

¹⁵Centro de Astrobiología (INTA-CSIC)

¹⁶Southwest Research Institute

¹⁷Los Alamos National Laboratory

November 24, 2022

Abstract

Mars 2020 Mars Environmental Dynamics Analyzer (MEDA) instrument data acquired during half of a martian year (L_s 139-180°), and modeling efforts with the Mars Regional Atmospheric Modeling System (MRAMS) and Mars Climate Database (MCD) allow us to study the seasonal evolution and variability of nocturnal atmospheric turbulence at Jezero crater. Nighttime conditions in Mars's Planetary Boundary Layer are highly stable because of strong radiative cooling that efficiently inhibits convection. However, MEDA nighttime observations of simultaneous, rapid fluctuations in horizontal wind speed and air temperatures suggest the development of nighttime turbulence in Jezero crater. Mesoscale modeling with MRAMS also shows a similar pattern and enables us to investigate the origins of this turbulence and the mechanisms at play. As opposed to Gale crater, less evidence of turbulence from breaking mountain/gravity wave activity was found in Jezero during the period studied with MRAMS. On the contrary, the model suggests that nighttime turbulence at Jezero crater is explained by mechanical turbulence produced by increasingly strong wind shear related to the development of a bore-like disturbance at the nocturnal inversion interface. The enhanced wind shear leads to a reduction in the Ri and an onset of mechanical turbulence. Once the

critical Richardson Number is reached ($Ri < 0.25$), shear instabilities can mix warmer air aloft down to the surface.

Hosted file

essoar.10512563.1.docx available at <https://authorea.com/users/250331/articles/603771-nocturnal-turbulence-at-jezero-crater-as-determined-from-meda-measurements-and-modeling>

Nocturnal turbulence at Jezero crater as determined from MEDA measurements and modeling

Jorge Pla-García¹, A. Munguira², S. Rafkin³, C. Newman⁴, T. Bertrand⁵, G. Martínez⁶, R. Hueso², A. Sánchez-Lavega², T. del Río Gaztelurrutia², A. Stott⁷, N. Murdoch⁷, M. de la Torre Juárez⁸, M. Lemmon⁹, B. Chide¹⁰, D. Viúdez-Moreiras¹, H. Savijarvi¹¹, M. Richardson⁴, M. Marín¹, E. Sebastian¹, A. Lepinette-Malvitte¹, L. Mora¹ and J.A. Rodríguez-Manfredi¹

¹Centro de Astrobiología (CAB), CSIC-INTA, Madrid, Spain; ²Universidad del País Vasco (UPV/EHU), Bilbao, Spain; ³Southwest Research Institute, Boulder, CO, USA; ⁴Aeolis Research, Chandler, AZ, USA; ⁵LESIA, Observatoire de Paris, France; ⁶Lunar and Planetary Institute, Houston, TX, USA; ⁷Institut Supérieur de l'Aéronautique et de l'Espace (ISAE-SUPAERO), Université de Toulouse, Toulouse, France; ⁸Jet Propulsion Laboratory, California Institute of Technology, Pasadena, CA, USA; ⁹Space Science Institute, Boulder, CO, USA;; ¹⁰Space and Planetary Exploration Team, Los Alamos National Laboratory, Los Alamos, New Mexico, USA; ¹¹Finnish Meteorological Institute, Helsinki, Finland

Corresponding author: Jorge Pla-García (jpla@cab.inta-csic.es)

Abstract

Mars 2020 Mars Environmental Dynamics Analyzer (MEDA) instrument data acquired during half of a martian year (L_s 13°-180°), and modeling efforts with the Mars Regional Atmospheric Modeling System (MRAMS) and Mars Climate Database (MCD) allow us to study the seasonal evolution and variability of nocturnal atmospheric turbulence at Jezero crater. Nighttime conditions in Mars's Planetary Boundary Layer are highly stable because of strong radiative cooling that efficiently inhibits convection. However, MEDA nighttime observations of simultaneous, rapid fluctuations in horizontal wind speed and air temperatures suggest the development of nighttime turbulence in Jezero crater. Mesoscale modeling with MRAMS also shows a similar pattern and enables us to investigate the origins of this turbulence and the mechanisms at play. As opposed to Gale crater, less evidence of turbulence from breaking mountain/gravity wave activity was found in Jezero during the period studied with MRAMS. On the contrary, the model suggests that nighttime turbulence at Jezero crater is explained by mechanical turbulence produced by increasingly strong wind shear related to the development of a bore-like disturbance at the nocturnal inversion interface. The enhanced wind shear leads to a reduction in the Ri and an onset of mechanical turbulence. Once the critical Richardson Number is reached ($Ri < 0.25$), shear instabilities can mix warmer air aloft down to the surface.

Key points

- Nocturnal turbulence at the rover's location in Jezero peaks at $L_s \sim 30^\circ$ and $L_s \sim 105^\circ$ - 180° in early northern summer, but is weakest shortly before this at $L_s \sim 90^\circ$.

- Periods of strong turbulence from 19:00-21:00 and at ~midnight
- Turbulence is produced by strong wind shear derived by local downslope winds from the west rim undercutting the regional easterly flow above (a strong jet at ~1-4 km height).

Plain Language Summary

The Martian atmosphere is very susceptible to turbulence. Its almost cloudless and very thin atmosphere combined with strong near-surface radiative heating produces strong near-surface unstable temperature gradients during the daytime, resulting in strong convective turbulence in the Mars planetary boundary layer. On the other hand, nighttime conditions near the surface are highly stable because of strong radiative cooling efficiently inhibiting convection, so turbulence is usually not expected. Nevertheless, during the nighttime, shear-driven, mechanically forced turbulence exists on Mars and is reported in this manuscript, using both Mars 2020 observations and modeling efforts.

Outline (to be removed if manuscript accepted for publication)

1. Introduction
2. Nighttime turbulence from Mars 2020 observations
3. Nighttime turbulence observed with modeling
4. Summary and Conclusions
5. Acknowledgements
6. Data Availability Statement
7. References
8. Supplementary Material

Introduction

The aim of this article is to explore the nocturnal and seasonal variability of atmospheric turbulence monitored by the Mars 2020 mission over half of a Martian year, from mission sol 15 corresponding to Mars areocentric solar orbital longitude, $L_s \sim 13^\circ$ (in early northern hemisphere spring) up to sol 362 corresponding to $L_s \sim 180^\circ$ (Northern fall equinox). Turbulent kinetic energy (hereafter TKE) in the planetary boundary layer (hereafter PBL) that measures the intensity of turbulence in a flow originates from two distinct sources: buoyancy and wind shear, since the other terms of the TKE equation simply redistribute TKE (Holton, 2004; Stull, 1988). Under Martian nighttime conditions, near-surface inversions act as a turbulence-suppressing buoyancy sink, hence wind shear is the only possible major source of local turbulence. Chatain et al. (2021) found that around perihelion ($L_s \sim 251^\circ$), shear-driven nighttime turbulence at the In-Sight landing site (located at Elysium Planitia, 4.5° N 135.6° E) is almost as

powerful as turbulence during the convective daytime, as a result of both the stronger ambient wind (low-level jet) and weaker stability. Rafkin et al. (2016) found that the rapid temperature fluctuations observed at night at Gale crater in all seasons is indicative of some mixing and nocturnal turbulence with the perturbations strongest at Ls 270 when northern crater rims trigger large amplitude strong breaking mountain waves bringing down warmer air and increasing heat flux.

The Mars 2020 Perseverance rover landed on Mars in February 2021 at 18.44°N; 77.45°E within and near the northwest rim of Jezero crater, a 45 km diameter impact crater located in the Nili Fossae region of Mars. Prior to Mars 2020’s landing, Pla-García et al. (2020) performed high-resolution meteorological simulations of Jezero crater at Ls 0°, 90°, 180°, and 270° and predicted strong nocturnal turbulence, especially at Ls~180°. In this study, we report observations of nocturnal turbulence made by Mars 2020’s Mars Environmental Dynamics Analyzer (MEDA) that confirm these pre-landing predictions, and use our original MRAMS simulations and additional ones at other Ls to interpret key periods observed in the first half of the Martian year. The Mars Regional Atmospheric Modeling System (MRAMS; Rafkin et al. 2001, 2002; Rafkin 2009; Rafkin and Michaels 2019) has previously demonstrated the ability to reproduce the observed meteorological conditions on Mars (Pla-Garcia et al. 2016), and here is applied to study the nighttime atmospheric turbulence conditions at the Mars 2020 Perseverance rover landing site inside Jezero crater for $L_s \sim 30^\circ, 60^\circ, 90^\circ, 105^\circ, 160^\circ$ and 180° , corresponding to Mars 2020 mission sols~51, 116, 182, 215, 325 and 361, respectively. MRAMS diurnal cycle results shown in section 3 are in good agreement with MEDA observations, and this agreement provides justification for utilizing the model results to investigate the nocturnal turbulence environment of the Jezero crater region. We have also used Mars Climate Database (MCD) results to provide global context for the MRAMS regional and local scale predictions (Millour et al. 2022). All times shown in observations and simulations are in LTST.

In Section 2, we briefly discuss the data from the sensors that were involved in this investigation. Section 3 presents modeling results regarding the development of nighttime local turbulence at Jezero crater and finally the Summary and Conclusions are presented in Section 4.

Nighttime turbulence from Mars 2020 observations

The MEDA data used in this analysis of nighttime atmospheric turbulence are provided by the Wind Sensors (WS), the Air Temperature Sensors (ATS) and the Thermal Infrared Sensor (TIRS) from the MEDA sensor suite (Rodríguez-Manfredi et al., 2021; Newman et al., 2022). Both WS and ATS can be operated with a measurement frequency up to 2 Hz, whereas TIRS is limited to a

frequency of 1 Hz. MEDA acquires data typically over 50% of a full sol, measure at odd hours during odd sols and even hours during even sols, so the combination of data from consecutive sols allows the study of timescales ranging from seconds to diurnal cycles and their seasonal evolution.

Wind data are taken by two WS on two booms located around the rover’s Remote Sensing Mast (RSM) at ~ 1.5 m height above the ground, separated $\sim 120^\circ$ from each other in the horizontal plane with boom 1 pointing 6° clockwise of the rover front. Two are needed to correct for the effects of thermal and mechanical interference by rover hardware, which disrupts winds approaching from different directions depending on the boom (Rodríguez-Manfredi et al., 2021). Measurements from both WS are compared and the boom least affected by rover hardware is identified and used to produce horizontal wind speed and direction values with an accuracy better than ± 1 m/s and a resolution of 0.5 m/s for wind speeds between 0-10 m/s, and 10% of the measurement and 0.1 m/s for wind speeds above 10 up to 40 m/s. The MEDA WS can also potentially characterize the vertical component of the wind for the first time, shedding light on atmospheric turbulence. Although no vertical winds are currently calculated, ongoing calibration efforts are aimed at retrieving those values. Only wind data from sols 15 to 313 ($L_s \sim 152^\circ$) are included in this study, because on sols 313 and 315 several boards of the WS were damaged due to wind-induced grain impacts, thus preventing high-accuracy wind retrievals since that time.

Air temperatures are measured by MEDA using five thermocouple sensors. Three of them (ATS-1, ATS-2, and ATS-3) are located on the RSM at 1.45 m above the ground, separated azimuthally $\sim 120^\circ$ from each other in the horizontal plane to ensure that at least one is always downwind from rover thermal interference. Two others (ATS-4 and ATS-5) are attached to the sides of the rover at a height of 0.84 m in order to shed light on the vertical temperature gradient close to the surface. All ATS have an accuracy and resolution better than 1 and 0.1 K, respectively (Rodríguez-Manfredi et al., 2021). ATS-1, ATS-2 and ATS-3 typically provide similar values and are less affected by the thermal influence of the rover compared to ATS-4 and ATS-5, which are closer to the rover body, its thermal influence, and less exposed to winds (Munguira et al., 2022).

TIRS is the first in-situ Martian IR radiometer including upward- and downward-looking channels (Rodríguez-Manfredi et al. 2021; Sebastián et al., 2020, 2021). TIRS measures the downwelling atmospheric IR flux (IR1), the air temperature from an atmospheric layer with peak emission at 40 m (IR2; Smith et al., 2006), the reflected (upwelling) solar flux (IR3), the upwelling IR flux emitted by the surface (IR4), and the surface brightness temperature (IR5) (Table 1). The TIRS air temperature data used in this analysis of nighttime atmospheric turbulence are provided by IR2.

Figure 1 shows MEDA fluctuations of derived horizontal TKE (hereafter TKE_H) and air temperatures at 1.5 m height averaged over specific local times during the first 362 sols of the mission. TKE_H at 1.5 m height is defined as:

$$\text{TKE}_H = \frac{1}{2} \left(\overline{(u')^2} + \overline{(v')^2} \right), \quad (1)$$

where u is the zonal component of the wind and v is the meridional component of the wind that is decomposed into a time average and a turbulent perturbation: $u = \bar{u} + u'$. MEDA data are divided into 5-minute windows and a polynomial fit of degree 2 is applied to the time series and extracted to get the fluctuations. We then calculate standard deviation of the fluctuations of each variable in the 5-minute window. Finally, we plot the average of the standard deviations over intervals of two-hours (19:00-21:00, 21:00-23:00, 23:00-01:00, 01:00-03:00 and 03:00-05:00) as a function of sol.

Note that the vertical component of the wind (w) in the TKE_H equation is not included as no information on the vertical component of the winds is currently available, as mentioned previously. In principle, the MEDA WS might be able to retrieve direct measurements of w and w' with better calibration. For the air temperature we only use measurements from ATS1 (black rod in Figures 2 and 3), as it is the one that is oriented towards the free atmosphere and is outside convective plumes from the rover's surface and more protected from the rover radioisotope thermoelectric generator (hereafter RTG), being located in the wake of the rover's mast wrt flows from that direction.

Figure 1 shows strong turbulence for the 19:00-21:00 and 21:00-23:00 periods, when both the TKE_H and 1.45 m air temperature fluctuations are correlated. After 03:00, only air temperature fluctuations are moderately large through the period, but TKE_H values remain low during the whole dataset with the exception of sol 311 ($L_s \sim 152^\circ$). Over all earlier times of night shown, there is a high turbulence period from sol 45 ($L_s \sim 27^\circ$) to sols 130 ($L_s \sim 66^\circ$) peaking around sols 75-80 ($L_s \sim 40^\circ$) and another during the summer starting at sol 215 ($L_s \sim 105^\circ$) peaking around sol 280 ($L_s \sim 136^\circ$). Between these seasonal peaks, there is a clear hiatus in turbulence centered roughly on summer solstice ($L_s \sim 90^\circ$) and lasting tens of sols, although this hiatus is shorter and centered earlier (at $L_s \sim 81^\circ$) in the period 01:00-03:00.

We carefully searched for relevant correlations of TKE_H fluctuations with air temperature fluctuations for the most promising periods of Figure 2. Not all of these periods are suitable for analysis because, depending on the rover's orientation and wind direction, temperature measurements may be perturbed by the rover's thermal boundary layer. Thermal plumes from the RTG can affect the air temperature measurements when the wind speed is between threshold values and blowing from the RTG toward the sensors (ATS-1 and ATS-3) located around the RSM (Gómez-Elvira, 2012; Lorenz & Sotzen, 2014). For this reason, a systematic analysis was performed to identify such periods of thermal contamination. Figure 2 shows the fluctuations of air temperature (at 0.85m, 1.45 m and ~ 40 m height) and wind speed and direction (at 1.5 m height) as observed by MEDA from 19:25 through 20:25 on sol 213 ($L_s \sim 104$), being a representative example in which we have a period with clear thermal contamination from the RTG and rover's deck as well as atmospheric turbulence, so it is an ideal illustration of the criteria used in our analysis to determine if the turbulence in

temperature is real:

- Atmospheric turbulence: Wind direction coming from the environment (from the S-SE in Figure 2 at ~19:46-19:56), without passing through the rover RTG or the rover deck. In many of these cases, ATS-1 measurements are correlated with ATS-5 and TIRS (both pointing in the same direction as ATS-1), and often coincide with TKE_H peaks. Usually, the ATS3 temperature signal does not fluctuate because it is downwind from the mast (Figure S1).
- RTG contamination: The winds come from a direction such that they reach the mast by passing through the RTG (from the SW in Figure 2 around ~19:40-19:45 and from the SSW in Figure 2 around ~20:15). ATS1 measurements are affected, although less than ATS-2 and ATS-3 (Figure S1). The measurements are not affected in ATS5, since it is lower and protected by the structure of the rover. TIRS measures some noise at most, but not being correlated with ATS-1. However, these thermal fluctuations are not accompanied by fluctuations in the winds that could cause a high value of TKE_H . Thus, environmental turbulence and artificially generated thermal fluctuations can be distinguished by comparison with the wind dataset. Simultaneous measurements of winds and temperatures are therefore key to determine if thermal perturbations caused by the rover and its RTG affect the temperature measurements at particular times (Davy et al., 2010).
- Deck contamination: The winds come in such a direction that they reach the mast passing through the deck (from the W-WN in Figure 2 around ~19:40-19:45). This is what introduces greater uncertainty since sometimes it is difficult to discern if the measurements are valid in each of the ATS. This does not mean that there is no temperature turbulence on these sols, but rather that we cannot isolate thermal contamination from the rover’s environment. Furthermore, this would introduce temperature fluctuations of the same order as the ones we are looking for (~4K), while those of the RTG are generally easier to identify because they produce signals up to ~10K (Munguira et al. 2022 this issue).

The clear correlations of rapid fluctuations observed in air temperatures and TKE_H in Figures 2 and 3 is a clear signature of nocturnal turbulence. A strong dependence of nocturnal turbulence on the ambient wind was also observed at InSight’s location (Chatain et al. 2021). Turbulent fluctuations in temperature in Jezero crater are explored further in other papers in this issue: using measurements from ATS (de la Torre-Juarez et al., 2022 this issue; Munguira et al., 2022 this issue) and the SuperCam microphone (Chide et al., 2022; this issue). More examples of the simultaneous fluctuations of surface and air temperature (at 0.85m, 1.45 m and ~40 m height) and wind speed and direction (at 1.5 m height) as observed by MEDA are shown in the Supplementary Material (Figures S1-S6).

MEDA bulk Richardson number

The Richardson number (Ri) is a dimensionless number that expresses the ratio of the buoyancy (Brunt–Väisälä frequency) to the wind shear as sources of turbulence:

$$Ri = \frac{N^2}{\left(\frac{\partial V}{\partial z}\right)^2}, \quad (2)$$

where N is the Brunt–Väisälä frequency and V is the horizontal wind speed. Ri helps interpret why the MEDA fluctuations of TKE_H and air temperature during nighttime have the observed variation with season shown in Figure 1. Negative Ri values point to a buoyancy source of turbulence during unstable conditions for daytime convective periods while positive Ri values indicate a buoyancy sink inhibiting turbulence in nighttime stable conditions (Stull, 1988). However, an initially laminar flow, for example, in a typical strongly stable nighttime conditions on Mars, may become turbulent for $0 < Ri < 0.25$. At this point, the wind-shear source of turbulence dominates the buoyancy sink producing nighttime turbulence, either because the wind shear is strong and/or because the stability is weak (Chatain et al. 2021).

Figure 4 shows a proxy of the bulk Richardson number, R_B , obtained along Perseverance’s traverse using MEDA measurements and similarity theory, as described in more detail in Martínez et al., 2022 (this issue):

$$R_B = \frac{g}{T_g} \frac{(T_a - T_g)z_a}{U_a^2}, \quad (3)$$

where g is gravitational acceleration, T_a is the air temperature at ~ 1.45 m, T_g is the surface brightness temperature, U_a is the horizontal wind speed at ~ 1.5 m measured by the MEDA WS and $z_a = 1.45$ is the height of the MEDA ATS. Eq. 3 assumes that the ground temperature (T_g) is representative of the very lowest atmospheric temperature. The regimes implied by certain values of R_B are “no turbulence” for R_B values > 1 , “stably-stratified weak turbulence” for $0.25 < R_B < 1$, “forced turbulence” for $0 < R_B < 0.25$ and “buoyancy-driven turbulence” for negative R_B values.

Based on Figure 4, it is clear that this region of Jezero crater is susceptible to turbulence during the night, with R_B values either negative or positive and below 0.25 most of the time, corresponding to shear-driven strongly turbulent regime. As expected, the R_B values remain negative (buoyancy-driven turbulence) during the daytime in all seasons shown here. The season most conducive to turbulence is $L_s \sim 105^\circ$, while the season at $L_s \sim 90^\circ$, with values of R_B above 0.25 between about 02:00 and 04:00, is least susceptible. $L_s \sim 30^\circ$ has lower R_B compared to $L_s \sim 60^\circ$. Based on Martínez et al. 2022 (this issue; section 4.2.3.), the unexpected negative values of MEDA bulk Richardson numbers after 04:00 at $L_s \sim 30^\circ$ and $L_s \sim 60^\circ$ and throughout most of the night at $L_s \sim 105^\circ$, could be produced by the apparent lack of a local thermal inversion, mostly occurred on sols with localized terrains with thermal inertia (TI) values higher than the mean values across Perseverance’s traverse obtained from MEDA ($TI > 350$ SI

units). The surface temperature used in the R_B equation of those sols is not representative as it is a very local measurement, while the air temperature is affected by a much larger terrain.

The SuperCam microphone has also observed significant midnight temperature fluctuations that are attributable to atmospheric turbulence (Mimoun et al. in review, Maurice et al. 2022). While, during the period analyzed in this paper (L_s 13°-180°), the microphone was mostly operated during the daytime, with only a handful of nighttime recordings, so coincident recordings of nocturnal turbulence were not made. Murdoch et al. (2022, submitted to Nature Communications) and Stott et al. (2022, this issue) found a definitive recording of nocturnal turbulence on sol 454 (L_s ~237°) just after midnight attributed to wind (Stott et al. 2022 this issue, Figure 2e). It confirms the observations in our work, as the results in Figure 1 show that 23:00-01:00 is the period with the greatest turbulence. Combining the sampling rate of MEDA with the high sampling rate of the microphone, the suite of sensors on Perseverance enables the characterization of nocturnal turbulence at a wider range of scales than before.

3. Nighttime turbulence observed with modeling

In an effort to better understand the turbulent nighttime environment inside Jezero crater, we use output from the MRAMS regional scale and MCD global scale models. A full description of the MRAMS model is included in Rafkin and Michaels (2019). For this study, MRAMS is configured with physics options and initialization similar to Pla-García et al. (2020) using seven grids with the innermost grids centered on the Mars 2020 Perseverance rover landing site location inside Jezero crater, Mars (77.45 °E, 18.44 °N) (Pla-García et al. 2020, Figure 1). The horizontal grid spacing at the center of the seven grids is 240, 80, 26.7, 8.9, 2.96, 0.98 and 0.33 km respectively. The lowest thermodynamic level in MRAMS is 14.5 m above the ground. Ideally, the first vertical level would be located at the MEDA instrument height (with sensors from 0.8 m to 1.5 m above the ground), but this is not computationally practical, as described in Pla-García et al. (2016). Output from the NASA Ames General Circulation Model (GCM) (Kahre et al., 2006) is used to initialize the atmospheric state in MRAMS. The output frequency is every five Mars minutes with output taken from the highest resolution grid. In order to obtain representative nighttime turbulent conditions to compare with MEDA data, the model was run for six solar longitudes, corresponding to the particular operational sols for Mars 2020 Perseverance rover, as shown in Table 1.

Modeled seasons and Corresponding Mars 2020 Operational sols

L_s	Operational Sol
30	51
60	116
90	182

Modeled seasons and Corresponding Mars 2020 Operational sols	
105	215
160	325
180	361

Table 1. *Modeled seasons and Corresponding MSL Operational sols*

MRAMS model validation with MEDA observational data

Air temperatures and wind speed and direction data obtained from MRAMS are compared to data from MEDA. A full diurnal cycle at six different times of year (L_s 30°, 60°, 90°, 105°, 160° and 180°) is investigated at the rover location within Jezero crater (Figures 5-8).

MRAMS vs MEDA air temperatures comparisons are shown in Figures 5 and 6. As expected, the MRAMS values at higher elevations tend to be cooler than observations in the morning and early afternoon, and then tend to be warmer in the late afternoon and through the night (Schofield et al., 1997). This is a direct result of the steep afternoon superadiabatic lapse rate and a strong nocturnal inversion (Schofield et al., 1997; Smith et al., 2004). During the day, the air temperature variations shown in the model and observations can be attributed to convective motions. The sudden increase in air temperature during the evenings at the onset of radiative cooling and the rapid air temperature fluctuations modeled at night in all times of the year (Figures 6 and 7) is indicative of nocturnal turbulence that could be mechanically driven (forcing warm air to descend or cold air to rise) since the atmosphere is stable and non-convective in the evening and at night.

Figure 7 show good match to wind directions between MRAMS and MEDA in most cases, but MRAMS wind speeds are generally higher than those observed with MEDA (Figure 8), especially between 23:00 and dawn. It is important to note that winds in the model are obtained from the lowest level at 14.5 m, whereas MEDA data are from an altitude of 1.5 m above surface. The small difference in height should not have a large impact on wind direction, but can contribute to the wind speed differences. Wind speeds at 14.5 m may be faster than at ~1.5 m due to frictional effects with the surface. It is not unreasonable that this height difference can explain a large fraction of the difference in wind speed, for example, under neutral conditions assuming a log wind profile between ~1.5 m and ~14.5 m, a 68% decrease on the wind speed is expected. Other contributions could include the uncertainty in the surface roughness, pressure gradient, errors in the model and/or in the observations, etc. Those wind speed differences are indeed bigger during nighttime, where MRAMS winds between 01:00 and sunrise could be so strong because the downslope winds penetrate a little bit too far into the crater for that time of sol when compared with other modeling predictions (Newman et al. 2021). It is also noticeable that the wind speeds are systematically extremely low about a couple hours after sunset both

in MRAMS and MEDA, following the collapse of daytime convection (Banfield et al. 2020), but then at 20:00 the wind speeds start to increase again both in modeling and observations.

Although there are some periods with differences, generally there is a good agreement between MRAMS results and MEDA observations, and this agreement provides justification for utilizing the model results to investigate the nocturnal turbulence environment of the Jezero crater region.

MRAMS Turbulence kinetic energy (TKE) results

As noted in the introduction, TKE measures the intensity of turbulence. The effect of subgrid-scale eddies is captured within MRAMS via a prognostic TKE equation (Mellor and Yamada 1974) in Figure 9. In MRAMS, TKE is the total turbulent kinetic energy that includes contributions from each of the 3D wind components (Mellor and Yamada, 1974). It may be interpreted as the energy contained in the dominant energy-carrying eddies that are too small to be resolved by the model. During convective periods, TKE is likely to include a substantial contribution from vertical motion. Thus, caution must be exercised when directly comparing MRAMS TKE to MEDA TKE_H .

The model does often show small increases of TKE during the night (Figure 9), especially at $L_s \sim 30^\circ$ (corresponding to Mars 2020 sol 51) and moreover from $L_s \sim 105^\circ$ to 180° (corresponding to Mars 2020 sols 216-362). Around midnight at $L_s \sim 160^\circ$ and $L_s \sim 180^\circ$ looks like there is a development of local turbulence with an amplitude as intense as its daytime counterpart. Also, noticeable is the moderate turbulence at $L_s \sim 30^\circ$ and the weak turbulence at $L_s \sim 60^\circ$ and 90° . During the late evenings and overnight, MRAMS often predicts rapid thermal variations, as shown in Figures 5 and 6. Examples include: $L_s \sim 60^\circ$ at $\sim 21:00$ and $\sim 03:00$; $L_s \sim 105^\circ$ from midnight to sunrise; $L_s \sim 160^\circ$ at $\sim 03:00$; and $L_s \sim 180^\circ$ from $\sim 01:00$ to $02:00$. The model often predicts increases of TKE at the same times as the thermal perturbations (Figure 9). This nighttime turbulence burst was *a priori* unexpected, given the aforementioned strong buoyancy sink for turbulence in Martian nights.

MRAMS Richardson number results

To investigate further the nighttime turbulence at Jezero crater with MRAMS, we calculate a Bulk Richardson Number from Eq (2) using the two lowest model levels at ~ 14.5 m and ~ 46 m.

Looking at Figure 10, it is clear that at $L_s \sim 30^\circ$ the environment is conducive to turbulence at around 19:00-19:30, 23:30-00:30 and then from 01:00 until sunrise with short periods lasting 5-15 min during which the Richardson number is very large nighttime turbulence is likely to be suppressed or absent. Because $N^2 > 0$ at night, we conclude that any turbulence will be mechanically forced. At $L_s \sim 60^\circ$ there is reduced Ri between 01:00 and 02:00 and between 03:30 and

sunrise. At $L_s \sim 90^\circ$ there is Ri between midnight and 03:00 and in some periods between 04:00 and sunrise, but there are also periods where the Richardson number is $\gg 0.25$. At $L_s \sim 105^\circ$ there is reduced Ri from sunset to 20:00 and from midnight to 03:00. At $L_s \sim 160^\circ$ there is occasional reduced Ri between 22:30 and midnight and persistently between 02:15 and 05:00. At $L_s \sim 180^\circ$ there are persistent low Ri values between 00:15 and 01:15 and between 03:00 and 05:00 with occasional reduced values between 01:15 and 02:15. Very strong ($Ri=0$) at 02:00. In the early hours of the night (19:00-20:00), the $L_s \sim 105^\circ$ is by far the season most susceptible to nocturnal turbulence, and at $\sim 03:00$ the environment is conducive to turbulence at $L_s \sim 30^\circ$, $L_s \sim 105^\circ$, $L_s \sim 160^\circ$ and $L_s \sim 180^\circ$.

MRAMS vertical profiles

MRAMS vertical profiles of wind magnitude, wind shear, Brunt-Väisälä frequency, Richardson number (Ri) and subgrid-scale TKE at Mars 2020 landing site for L_s 30° , 60° , 90° , 105° , 160° and 180° are shown in Figure 11. All values are averaged over the five-time ranges shown: 19:00-21:00, 21:00-23:00, 23:00-01:00, 01:00-03:00 and 03:00-05:00. Ri is out of range in Figure 11 for most of the altitude range, as we have limited the range to -0.25 to 1.25 in order search for nighttime environments conducive to turbulence. The whole range of Ri is included in Figure S7.

Once the critical Richardson Number is reached ($Ri \lesssim 0.25$), shear instabilities can mix warmer air aloft down to the surface, something observed with MEDA. Air temperature data show night-time pulses of warm air that are due to atmospheric turbulence (not created by rover perturbation), as determined by there being correlations between TKE_H and winds as in the examples in Figures 2 and 3.

Description of the MRAMS nighttime turbulence shown in Figure 11 for the six different times of year studied:

- $L_s \sim 30^\circ$ has moderate nighttime turbulence. The most interesting period of the night, unlike the other times of year considered, is after midnight, with Ri decreasing from 23:00 to 05:00. Wind shear is strongest late in the night before sunrise, between 01:00 and 05:00. Wind shear is very low during the first part of the night, from 19:00 to 23:00. The turbulence in this period of the year is stronger than at $L_s \sim 60^\circ$ and $\sim 90^\circ$.
- $L_s \sim 60^\circ$ has low nighttime turbulence, especially in the period around midnight, between 23:00 and 01:00. However, weak turbulence can be seen in the first part of the night, around 19:00-21:00 and also before sunrise, between 03:00 and 05:00. That is, we have the presence of weak turbulence in the early and late hours of the night and no turbulence during the rest of the period. The wind shear is strongest before sunrise, between 03:00 and 05:00, and moderate or very low during the rest of the night.
- $L_s \sim 90^\circ$ has the least nighttime turbulence, with an absence of turbulence throughout the night.

- $L_s \sim 105^\circ$ is a high turbulent period, with strong turbulence produced by a strong wind shear after midnight and before sunrise, from 01:00-03:00 and 03:00-05:00, and with moderate turbulence from 19:00-21:00 and 23:00-01:00.
- $L_s \sim 160^\circ$ and $\sim 180^\circ$ also have strong turbulence caused by wind shear, but this is contained exclusively to the period before sunrise, i.e., from 03:00-05:00. There is also some turbulence in the first moments of the night (19:00-21:00) but some hundreds of meters above surface.

The strongest wind shear in Figure 11 always occurs in the period before sunrise, between 03:00 and 05:00, followed by the period 01:00-03:00 (especially for $L_s \sim 30^\circ$ and $\sim 105^\circ$). The weakest Brunt-Väisälä frequency occurs between 19:00-21:00 except at $L_s \sim 180^\circ$, which values between 23:00-01:00 are indeed lower. There are also some interesting peaks of TKE around ~ 300 m above the surface at all seasons. The clear near-surface stable inversions inhibit vertical mixing; hence wind shear is the only source of turbulence.

The origin of this nocturnal turbulence is explored using cross sections of MRAMS model output. Figures 12-15 show vertical slices from west to east across Jezero crater at Mars 2020 latitude (18.44°N) at 18:00, 20:00, 00:00 and 04:00 (and for a whole sol in the animations included in the Supplementary Material) as a function of all seasons, from MRAMS grid #7.

Jezero crater is embedded inside and close to the NW rim of the Isidis basin, whose daytime regional upslope (east-southeasterly) and nighttime regional downslope (northwesterly) winds dominate (Newman et al. 2021). Animations (Supplementary Material) show strong regional upslope winds developing during daytime towards the west rim of Jezero crater. At night, local downslope flow develops from the west rim of Jezero crater and undercuts the residual upslope winds (Figure 13). Looking at wind magnitudes on Figure 11 (left panels), the strongest jet is generally found from 19:00-21:00. It is even stronger before sunset at 18:00 (Figure 12). In Figures 13-15 there is an extremely strong shear, i.e., a strong low-level jet of about 20 m/s at about 1-4 km height, which produces instabilities that can mix air aloft down to the surface producing the turbulence observed by the rover between 19:00 and 03:00. As time goes on through the night, the magnitude of the jet decreases (left panels of Figure 11, Figures 13-15) as it does MEDA TKE_H in Figure 1.

For many of the periods of the year, the local downslope front from the west rim appears to take the form of a bore wave (Figure 13, especially). Bore waves have been suspected to exist on Mars based on imagery (Hunt et al. 1981) and modeling (Sta. Maria et al, 2006). A key environmental factor allowing bore propagation is the presence of a low-level jet directed opposite to the movement of the bore (Haghi and Durran 2021), as shown in Figures 13 and 14. The passage of this wave is likely the cause of the turbulence in the late evening, and, importantly, it is different than the breaking mountain waves suggested

for Gale crater (Rafkin et al. 2016). Compared to Gale crater, there is lower evidence of significant mountain/gravity wave activity in Jezero crater during the whole period studied with MRAMS.

Based on the model results, the low Ri values are due to an increase in wind shear between the low-level local downslope wind from the west rim behind the bore and the regional easterly (westward) flow above (a strong jet at ~1-4 km height). The downslope front propagates from the crater rim toward the interior basin, like a bore wave. That local downslope flow undercutting the easterly flow above enhances the wind shear, and this leads to a reduction in the Ri and the onset of mechanical turbulence; that is essentially how why bores produce turbulence in their wake. Significant turbulence is developed in the layer between the jet maximum and the surface (Haghi and Durran 2021). Once the critical Richardson Number is reached ($Ri \lesssim 0.25$), shear instabilities can mix warmer air aloft down to the surface (Miles 1961; Spiga & Forget 2009; Banfield et al. 2020). This turbulent mixing process has been observed in the Owens Valley (USA) under similar katabatic wind conditions emanating from the Sierra Mountains (Whiteman, 1982; Whiteman and Doran, 1993).

Contributions of the large-scale to Jezero crater turbulence

Although the spatial resolution of the general circulation model Mars Climate Database (MCD) output is $\sim 5.625 \times 3.75^\circ$ (longitude x latitude, therefore Jezero crater is not resolved and output are interpolated from the nearest grid points), it remains a useful tool to provide additional context to explain the atmosphere dynamics in the region of Jezero crater.

A nighttime low-level regional (~1-4 km height) easterly (westward) jet is also present in the MCD (Figure 16) and corresponds to a large-scale circulation feature forced by the diurnal cycle and the large-scale collapse of the PBL, provided that these models have a good parameterization of the PBL mixing. This large-scale feature contributes to the overall wind field which is dominated by the local scale circulation at Jezero crater. Undercutting of the downslope winds through Jezero crater west rim from the regional easterly flow above is producing the shear.

By using the MCD, we can see that the low-level (1-4 km) zonal winds near Jezero first reverse at sunset (they are eastward during the day, then westward during the night) and then this low-level westward jet intensifies during nighttime (Figure 16). This change in wind direction and the subsequent intensification of the low-level jet may be the result of different factors. First, the region is adjacent to Syrtis Major, a large-scale ~1,000 km² region with (1) a low surface albedo, which causes surface temperatures to be warmer hence an enhanced radiative heating in the infrared, and (2) high-elevated terrains, both effects leading to a more vigorous PBL in this region (see Figure 16 in

Colaïtis et al., 2013). The MCD predicts a large 10 km maximal PBL height in the afternoon in the vicinity of Syrtis Major, which is roughly 30% larger than what is predicted in the surrounding regions. The large-scale collapse of the PBL in this region should therefore lead to intense pressure changes with longitude and intense changes in vertical mixing during PBL collapse, favoring changes in wind direction and likely a strong low-level jet, as obtained with the MCD and MRAMS in Jezero crater region. Second, slopes are large in Syrtis Major and in the vicinity of Jezero crater, and slope winds could contribute to change the wind direction at sunset as well. For instance, slope winds (even on a gentle slope) strongly control the inversion in wind direction at Insight landing site (Banfield et al., 2020). These two factors may combine and dominate to explain the low-level wind direction at night, although other factors could combine together and contribute such as large-scale circulation and global tide effects. All these factors can also impact the local intensity of the low-level jet at night. In Figure 16, we show the horizontal zonal winds at the rover’s location as obtained with the MCD, for 1 km, 2 km, 3km and 4 km height over an entire year. A stronger westward low-level jet is produced at all seasons during nighttime, in particular during the first part of the night (19:00-01:00) in the period $Ls\sim 60^{\circ}$ - 180° , also observed in the MRAMS wind magnitude panels of Figure 11 and on Figures 12-15.

Figures 17-18 show the diurnal and seasonal variations of the Richardson number as extracted from the MCD at Mars 2020 location, using a climatological time-evolving 3D dust distribution (i.e. averages over many years without global dust storms). Wind speed values have been taken at 5 m and 10 m above the surface due to the vertical resolution of the MCD, as in Chatain et al., (2021), which is low enough to estimate the wind shear intensity near the rover. According to the MCD, nighttime turbulence should peak at $Ls\sim 105^{\circ}$ and always between 19:00 and 23:00 and between 03:00 and sunrise, which is in agreement with our results. The MCD predicts more shear-driven turbulence after sunset during the periods $Ls\sim 90^{\circ}$ - 130° (19:00-00:00), and $Ls\sim 130^{\circ}$ - 180° (03:00-05:00), in agreement with MRAMS results (Figure 11).

Summary and Conclusions

Nighttime observations of rapid horizontal wind and air temperature fluctuations by MEDA sensors show the development of nocturnal local turbulence in Jezero crater. MRAMS results are shown to be in good agreement with MEDA observations, and this agreement provides justification for utilizing the model results to investigate the origin of the nocturnal turbulence environment of the Jezero crater region and the mechanisms at play.

As derived both from observations and modeling, nocturnal turbulence at the rover’s location in Jezero crater peaks at $Ls\sim 30^{\circ}$ and $Ls\sim 105^{\circ}$ - 180° in early northern summer, but is weakest shortly before this at $Ls\sim 90^{\circ}$. Interesting periods of high nocturnal turbulence occur at 19:00-21:00 and around midnight.

Based on model results, the enhanced mechanical nighttime turbulence at Jezero crater can be attributed to low-level local downslope winds from the west rim (that appears to take the form of a bore wave) undercutting the regional easterly (westward) flow above (a strong jet at $\sim 1\text{-}4$ km height), enhancing the wind shear and leading to a reduction in the Ri and an onset of mechanical turbulence. Once the critical Richardson Number is reached ($\text{Ri} \lesssim 0.25$), shear instabilities mix warmer air aloft down to the surface. The large-scale circulation may set the conditions but they are not sufficient to explain the turbulence that is observed locally at Jezero crater. As opposed to Gale crater, less evidence of significant mountain/gravity wave activity was found in Jezero crater during the period studied with MRAMS.

The SuperCam microphone has also observed significant midnight temperature fluctuations which are attributable to atmospheric turbulence, founding a definitive recording of nocturnal turbulence on sol 454 ($L_s \sim 237^\circ$) just after midnight. Although this is outside the period analyzed in this paper, it fits very well with our work, as our results show that 23:00-01:00 is the period with the greatest turbulence.

Our results demonstrate that the continuous high-frequency atmospheric measurements by Mars 2020 MEDA sensors are key to unveiling the properties of Martian nighttime turbulence, and provide valuable data for testing and refining the physics involved, as encapsulated within atmospheric models. Similarly, models of the atmospheric circulation in Jezero crater are valuable for interpreting these data.

Figures uploaded separately. Figures captions:

Figure 1. *MEDA TKE_H and fluctuations in air temperatures at 1.45 m height as a function of sol number through the mission, for five nighttime observation periods.*

Figure 2. *(left) The rover orientation for this period and placement of the five ATS (ATS-1 and ATS-5 colorized as in the upper right-hand plot), to aid in analyzing thermal contamination from the rover's RTG and deck. (right) MEDA data from 19:25 through 20:25 on sol 213 ($L_s 104$), showing (top) 0.85m ATS-5 air temperatures (light blue line), 1.45m ATS1 air temperatures (black line), and $\sim 40\text{m}$ air temperature (cream line), and (bottom) wind direction (purple line), wind speed (black dots) and TKE_H (light blue line, derived from MEDA wind speeds as shown in the text) fluctuations.*

Figure 3. *Same as Figure 3 but for sol 85 ($L_s 45$) from 19:00-20:00.*

Figure 4. *MEDA bulk Richardson number diurnal timeseries over five sols at each of four times of year. Also indicated to the right is the regime implied by different values of R_B .*

Figure 5. *MEDA air temperature at ~ 1.45 m measured by the ATS within five sols of the given L_s (blue curves) and MRAMS data taken from the lowest model level at 14.5 m (solid black curve).*

Figure 6. Same as Figure 5, but comparing MEDA air temperature at ~ 40 m measured by TIRS and MRAMS data taken from the second model level at 46 m.

Figure 7. Same as Figure 5, but for wind directions. Note that the MEDA WS stopped working after sol 313, so we only have MEDA wind data to compare with for $Ls \sim 30^\circ$, 60° , 90° and 105° .

Figure 8. Same as Figure 7, but for wind speeds.

Figure 9. Two sols timeseries of Turbulent Kinetic Energy predicted with MRAMS for Mars 2020 landing site for Ls 30° , 60° , 90° , 105° , 160° and 180°

Figure 10. MRAMS Richardson number diurnal timeseries at ~ 14.5 m height at Mars 2020 landing site for Ls 30° , 60° , 90° , 105° , 160° and 180°

Figure 11. MRAMS vertical profiles of wind magnitude, wind shear, Brunt-Väisälä frequency, Richardson number (Ri) and subgrid-scale TKE at Mars 2020 landing site for Ls 30° , 60° , 90° , 105° , 160° and 180°

Figure 12. MRAMS model cross-section of winds and TKE at 18:00 of Ls 30° , 60° , 90° , 105° and 180° . Jezero's west rim is on the left and east rim on the right. Total horizontal wind in colored shadowed. Winds are also shown with white arrows in which the vertical component has been increased $\times 5$. Values of TKE are shown in black contours with black and white labels for each contour. The Perseverance rover landing site location corresponds to $x = 17.5$

Figure 13. Same as Figure 12 but for 20:00.

Figure 14. Same as Figure 12 but for 00:00.

Figure 15. Same as Figure 12 but for 04:00.

Figure 16. Diurnal cycle of horizontal eastward (+) and westward (-) winds at Mars 2020 location as obtained with the Mars Climate Database, for 1 km, 2 km, 3km and 4 km height over an entire year. Zonal winds averaged over many quiet years.

Figure 17. Richardson number at Jezero crater as extracted from the Mars Climate Database (MCD).

Figure 18. Diurnal variations of the Richardson number computed from the Mars Climate Database at 5 m above the surface in the conditions of the Mars 2020 landing site for the nine seasons.

Acknowledgements

This research has been funded by grant No. RTI2018-098728-B-C31 by the Spanish Ministry of Science and Innovation/State Agency of Research MCIN/AEI/ 10.13039/501100011033. AM, ASL, TR and RH were supported by grant PID2019-109467GB-I00 funded by MCIN/AEI/10.13039/501100011033/

and by Grupos Gobierno Vasco IT1366-19. Part of this research was carried out at the Jet Propulsion Laboratory, California Institute of Technology, under a contract with the National Aeronautics and Space Administration (80NM0018D0004). The JPL co-authors acknowledge funding from NASA's Space Technology Mission Directorate and the Science Mission Directorate. CEN was supported by funding from the Mars 2020 mission, part of the NASA Mars Exploration Program.

Data Availability Statement

All Mars 2020 MEDA data necessary to reproduce each figure shown in this manuscript are available via the Planetary Data System (PDS) Atmospheres node as the Mars Environmental Dynamics Analyzer (MEDA) Experiment Data Record (EDR) and Reduced Data Record (RDR) Data Products Archive Bundle (J.A.Rodriguez-Manfredi et al. 2021, doi: 10.17189/1522849).

References

- D. Banfield, A. Spiga, C. Newman, F. Forget, M. Lemmon, R. Lorenz et al., The atmosphere of Mars as observed by InSight. *Nat. Geosci.* 13, 190–198 (2020)
- A.K. Blackadar, Boundary layer wind maxima and their significance for the growth of nocturnal inversions. *Bull. Am. Meteorol. Soc.* 38(5), 283–290 (1957)
- Chatain, A., Spiga, A., Banfield, D., Forget, F., & Murdoch, N. (2021). Seasonal variability of the daytime and nighttime atmospheric turbulence experienced by InSight on Mars. *Geophysical Research Letters*, 48(22), e2021GL095453.
- Chide B., T. Bertrand, R. D. Lorenz, A. Munguira, R. Hueso, A. Sánchez-Lavega, ...other (2022). Acoustics reveals short-term air temperature fluctuations near Mars' surface. *Geophysical Research Letters*, submitted to this issue.
- Colařtis, A., Spiga, A., Hourdin, F., Rio, C., Forget, F., & Millour, E. (2013). A thermal plume model for the Martian convective boundary layer. *Journal of Geophysical Research: Planets*, 118(7), 1468-1487.
- P.A. Davis, Development and mechanisms of the nocturnal jet. *Meteorol. Appl.* 7(3), 239–246 (2000)
- Davy, R., Davis, J. A., Taylor, P. A., Lange, C. F., Weng, W., Whiteway, J., & Gunnlaugson, H. P. (2010). Initial analysis of air temperature and related data from the phoenix met station and their use in estimating turbulent heat fluxes. *Journal of Geophysical Research: Planets*, 115(E3).
- de la Torre Juárez, M., A. Chavez, L. K. Tamppari, A. Munguira, G. Martínez, R Hueso, ... other (2022). Diurnal cycle of air temperature fluctuations at Jezero

crater. *J. Geophys. Res.*, submitted to this issue.

Gómez-Elvira, J., Armiens, C., Castñer, L., Domínguez, M., Genzer, M., Gómez, F., . . . Martín-Torres, J. (2012). REMS: The Environmental Sensor Suite for the Mars Science Laboratory Rover. *Space Sci. Rev.*, 170 (1-4), 583-640. doi: 10.1007/s11214-012-9921-1

Guo, X., W.G. Lawson, M.I. Richardson and A.D. Toigo, Fitting the Viking lander surface pressure cycle with a Mars General Circulation Model, *J. Geophys. Res.*, 114, E07006, doi:10.1029/2008JE003302, 2009.

Haghi, K. R., & Durran, D. R. (2021). On the dynamics of atmospheric bores. *Journal of the Atmospheric Sciences*, 78(1), 313-327.

Hunt, G.E., Pickersgill, A.O., James, P.B., Evans, N., 1981. Daily and seasonal Viking observations of martian bore wave systems. *Nature* 293, 630–633.

M.A. Kahre, J.R. Murphy, R.M. Haberle, Modelling the Martian dust cycle and surface dust reservoirs with the NASA Ames general circulation model. *J. Geophys. Res.*, Planets 111(6), E06008 (2006)

Lorenz, R. D., & Sotzen, K. S. (2014). Buoyant thermal plumes from planetary landers and rovers: application to sizing of meteorological masts. *Planetary and Space Science*, 90, 81-89.

L. Mahrt, The early evening boundary layer transition. *Q. J. R. Meteorol. Soc.* 107(452), 329–343 (1981)

G.M. Martínez, C.N. Newman, A. De Vicente-Retortillo, E. Fischer, N.O. Renno, M.I. Richardson et al., The modern near-surface Martian climate: a review of in-situ meteorological data from Viking to Curiosity. *Space Sci. Rev.* 212(1–2), 295–338 (2017)

G. M. Martínez, E. Sebastián, A. Vicente-Retortillo, M. D. Smith, J. R. Johnson, E. Fischer, ... others (2022). Surface Energy Budget, Albedo and Thermal Inertia at Jezero Crater, Mars, as Observed from the Mars 2020 MEDA Instrument. *J. Geophys. Res.*, submitted to this issue.

G. Mellor, T. Yamada, A hierarchy of turbulence closure models for planetary boundary layers. *J. Atmos. Sci.* 31, 1791–1806 (1974)

J.W. Miles, On the stability of heterogeneous shear flows. *J. Fluid Mech.* 10(4), 496–508 (1961)

Millour, E. et al., The Mars Climate Database, Version 6.1, in *Seventh International Workshop on the Mars Atmosphere: Modelling and Observations*, 2022.

Munguira A., R. Hueso, A. Sanchez-Lavega, M. de la Torre-Juarez, G. Martinez, C. E. Newman, ... other (2022). Near Surface Atmospheric Temperatures at Jezero from Mars 2020 MEDA measurements. *J. Geophys. Res.*, submitted to this issue.

- N. Murdoch, A. E. Stott, M. Gillier, R. Hueso, M. Lemmon, G. Martinez, ... other (2022). The Sound of a Martian Dust Devil. Submitted to Nature Communications
- Newman, C. E., Hueso, R., Lemmon, M. T., Munguira, A., Vicente-Retortillo, Á., Apestigue, V., ... & Guzewich, S. D. (2022). The dynamic atmospheric and aeolian environment of Jezero crater, Mars. *Science Advances*, 8(21), eabn3783. Petrosyan et al., 2011
- Newman, C. E., De La Torre Juarez, M., Pla-García, J., Wilson, R. J., Lewis, S. R., Neary, L., ... & Rodriguez-Manfredi, J. A. (2021). Multi-model meteorological and aeolian predictions for Mars 2020 and the Jezero Crater Region. *Space science reviews*, 217(1), 1-68.
- Pla-García, J., Rafkin, S. C., Martinez, G. M., Vicente-Retortillo, Á., Newman, C. E., Savijärvi, H., ... & Harri, A. M. (2020). Meteorological predictions for Mars 2020 Perseverance Rover landing site at Jezero crater. *Space science reviews*, 216(8), 1-21.
- Pla-Garcia, S.C.R. Rafkin, M. Kahre, J. Gomez-Elvira, V.E. Hamilton, S. Navarro, J. Torres, M. Marín, A.R. Vasavada, The meteorology of Gale crater as determined from rover environmental monitoring station observations and numerical modeling. Part I: comparison of model simulations with observations. *Icarus* 280, 103–113 (2016). <https://doi.org/10.1016/j.icarus.2016.03.013>
- S.C.R. Rafkin, A positive radiative-dynamic feedback mechanism for the maintenance and growth of Martian dust storms. *J. Geophys. Res.* 114, E01009 (2009)
- S. Rafkin, T. Michaels, The Mars Regional Atmospheric Modeling System (MRAMS): current status and future directions. *Atmosphere* 10(12), 747 (2019)
- S.C.R. Rafkin et al., The meteorology of Gale Crater as determined from Rover Environmental Monitoring Station observations and numerical modeling. Part II: interpretation. *Icarus* 280, 114–138 (2016)
- S.C.R. Rafkin, M.R.V. Sta Maria, T.I. Michaels, Simulation of the atmospheric thermal circulation of a martian volcano using a mesoscale numerical model. *Nature* 419, 697–699 (2002)
- S.C.R. Rafkin, R.M. Haberle, T.I. Michaels, The Mars Regional Atmospheric Modeling System (MRAMS): model description and selected simulations. *Icarus* 151, 228–256 (2001)
- Rodriguez-Manfredi, J. A., De la Torre Juárez, M., Alonso, A., Apéstigue, V., Arruego, I., Atienza, T., ... & Zurita, S. (2021). The Mars Environmental Dynamics Analyzer, MEDA. A suite of environmental sensors for the Mars 2020 mission. *Space science reviews*, 217(3), 1-86.

- Schofield, J.T., Barnes, J.R., Crisp, D., et al., 1997. The Mars pathfinder atmospheric structure investigation/meteorology (ASI/MET) experiment. *Science* 278 (5344), 1752–1758.
- Smith, M.D., Wolff, M.J., Lemmon, M.T., et al., 2004. First atmospheric science results from the Mars exploration rovers mini-TES. *Science*: 306 (5702), 1750–1753.
- Spiga, A., & Forget, F. (2009). A new model to simulate the Martian mesoscale and microscale atmospheric circulation: Validation and first results. *Journal of Geophysical Research: Planets*, 114(E2).
- Sta. Maria, M., Rafkin, S.C. and Michaels, T.I., 2006. Numerical simulation of atmospheric bore waves on Mars. *Icarus*, 185(2), pp.383-394.
- Stott A. E., N. Murdoch, M. Gillier, D. Banfield, T. Bertrand, B. Chide, ... others (2022). Wind and turbulence observations with the Mars microphone on Perseverance. *J. Geophys. Res.*, submitted to this issue.
- Stull, R. (1988). *An introduction to boundary layer meteorology*. Kluwer Academic Publishers.
- Thorpe, A. J., & Guymer, T. H. (1977). The nocturnal jet. *Quarterly Journal of the Royal Meteorological Society*, 103(438), 633-653.
- Tillman, J. E., Landberg, L., & Larsen, S. E. (1994). The boundary layer of Mars: Fluxes, stability, turbulent spectra, and growth of the mixed layer. *Journal of the Atmospheric Sciences*, 51(12), 1709-1727.
- Van de Wiel, B. J., Moene, A. F., Steeneveld, G. J., Baas, P., Bosveld, F. C., & Holtslag, A. A. M. (2010). A conceptual view on inertial oscillations and nocturnal low-level jets. *Journal of the atmospheric sciences*, 67(8), 2679-2689.
- Whiteman, C. D. (1982). Breakup of temperature inversions in deep mountain valleys: Part I. Observations. *Journal of Applied Meteorology and Climatology*, 21(3), 270-289.
- Whiteman, C. D., & Doran, J. C. (1993). The relationship between overlying synoptic-scale flows and winds within a valley. *Journal of Applied Meteorology and Climatology*, 32(11), 1669-1682.

Supporting Information for

Nocturnal turbulence at Jezero driven by the onset of a low-level jet as determined from MEDA measurements and modeling

Jorge Pla-García¹, A. Munguira², S. Rafkin³, C. Newman⁴, T. Bertrand⁵, G. Martínez⁶, R. Hueso², A. Sánchez-Lavega², T. del Río Gaztelurrutia², A. Stott⁷, N. Murdoch⁷, B. Chide⁷, M. de la Torre Juárez⁸, M. Lemmon⁹, D. Viúdez-Moreiras¹, H. Savijarvi¹⁰, M. Richardson⁴, M. Marín¹, E. Sebastian¹, A. Lepinette-Malvitte¹, L. Mora¹ and J.A. Rodríguez-Manfredi¹

¹Centro de Astrobiología (CAB), CSIC-INTA, Madrid, Spain; ²Universidad del País Vasco (UPV/EHU), Bilbao, Spain; ³Southwest Research Institute, Boulder, CO, USA; ⁴Aeolis Research, Chandler, AZ, USA; ⁵LESIA, Observatoire de Paris, France; ⁶Lunar and Planetary Institute, Houston, TX, USA; ⁷ISAE-SUPAERO, Université de Toulouse, 31055 Toulouse, France; ⁸Jet Propulsion Laboratory, California Institute of Technology, Pasadena, CA, USA; ⁹Space Science Institute, Boulder, CO, USA; ¹⁰Finnish Meteorological Institute, Helsinki, Finland.

Contents of this file

Figures S1 to S7.

Additional Supporting Information (Files uploaded separately)

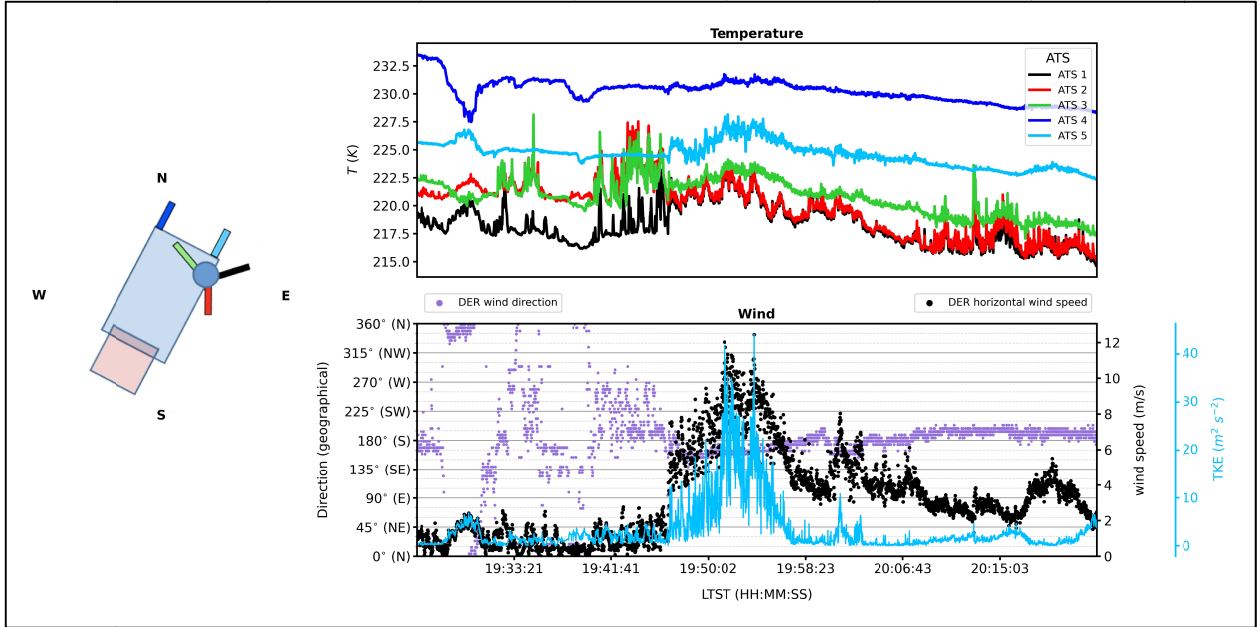
The MRAMS atmospheric circulation animations associated with nocturnal turbulence at Jezero can be found, in the online version, at:

https://data.boulder.swri.edu/jpla/Jezero_nocturnal_turbulence_movies/

Readme file describes the content of each animation like x-y axis labels, Mars 2020 Perseverance rover landing site location inside Jezero crater (77.45°E, 18.44°N), etc.

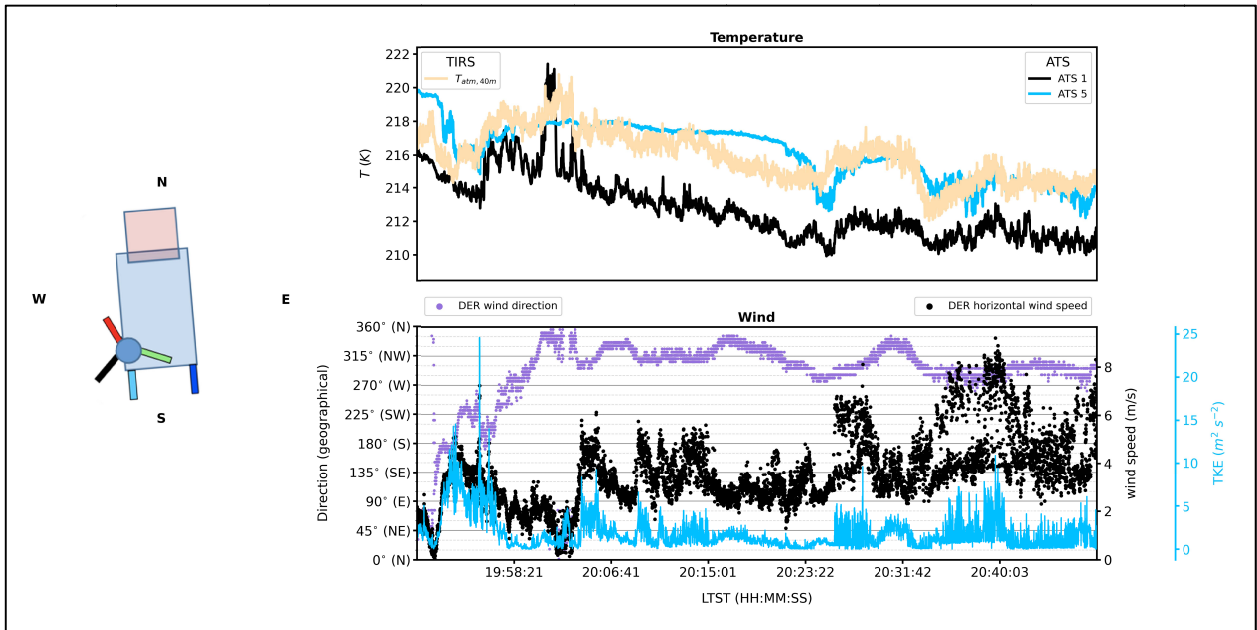
Introduction

The supporting information for this manuscript includes ten figures (Figs. S1 to S7, shown below).



26
27
28

Figure S1. Same as Figure 3 but including all ATS sensors (ATS-1 to ATS-5).



29
30
31

Figure S2. Same as Figure 3 but for sol 60 (L_s 34) from 19:50-20:50.

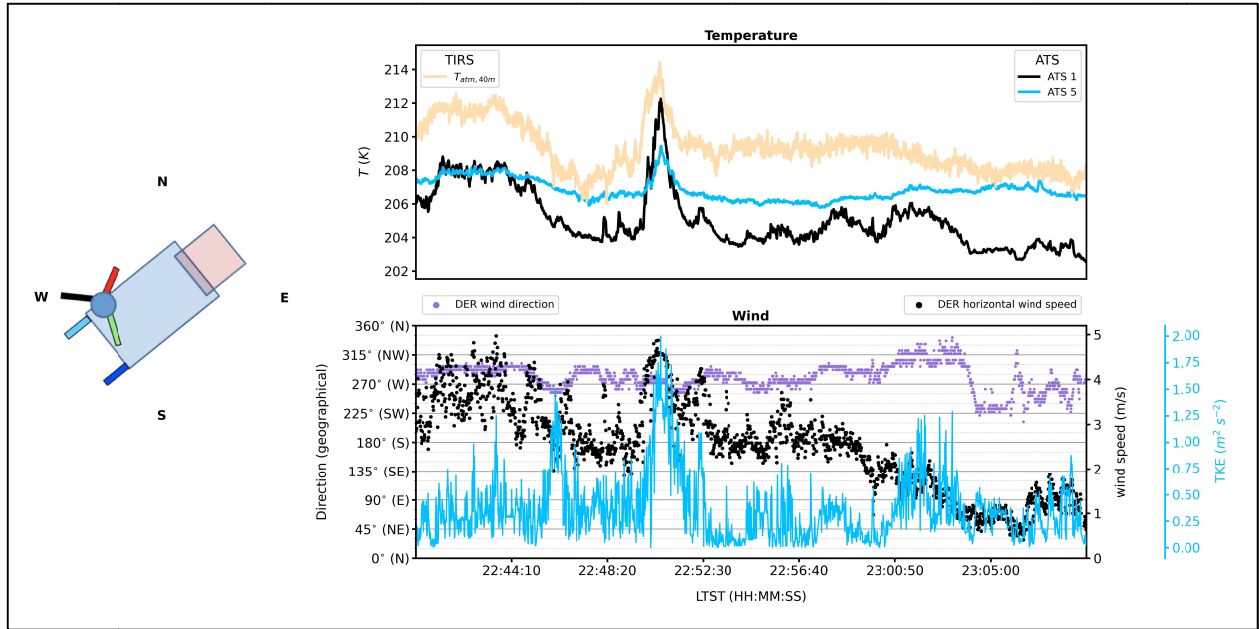


Figure S3. Same as Figure 3 but for sol 308 (L_s 150) from 22:40-23:10.

32
33
34
35

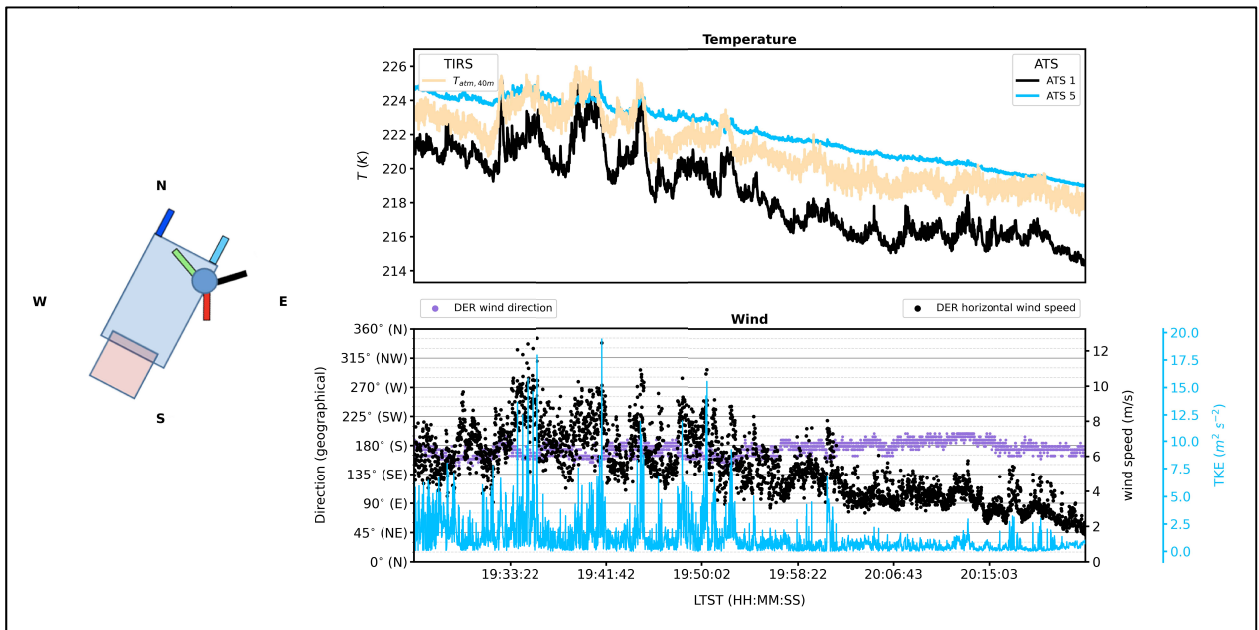


Figure S4. Same as Figure 3 but for sol 211 (L_s 102) from 19:25-20:25.

36
37
38
39

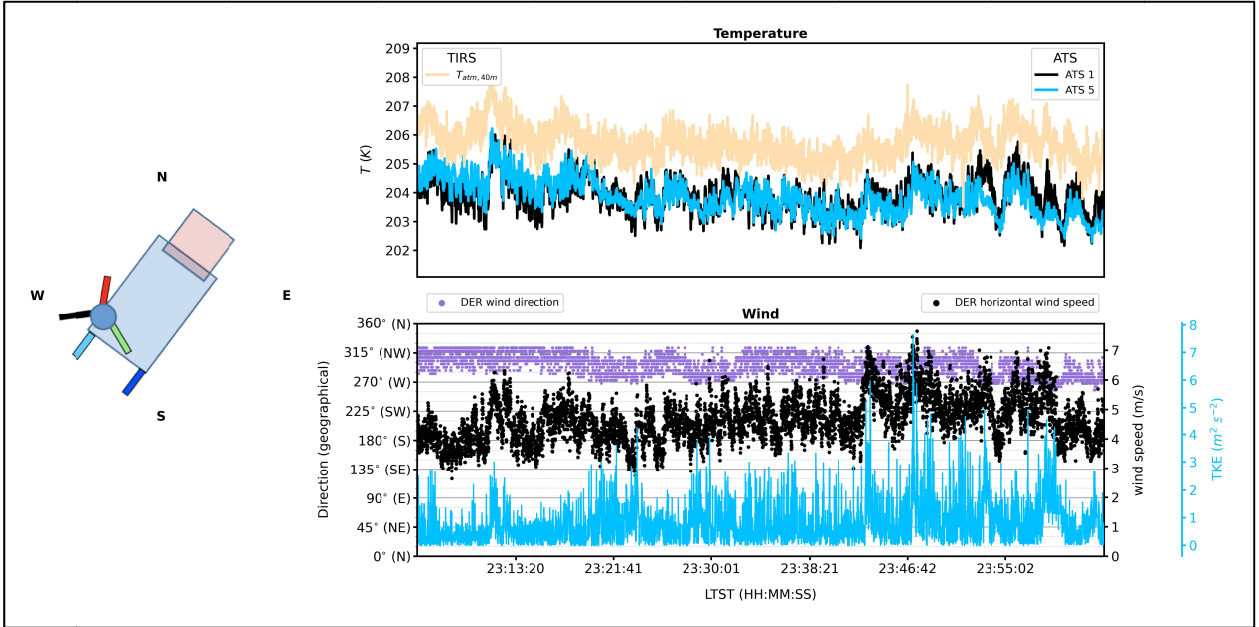


Figure S5. Same as Figure 3 but for sol 109 (*Ls* 56) from 23:05-00:05.

40
41
42

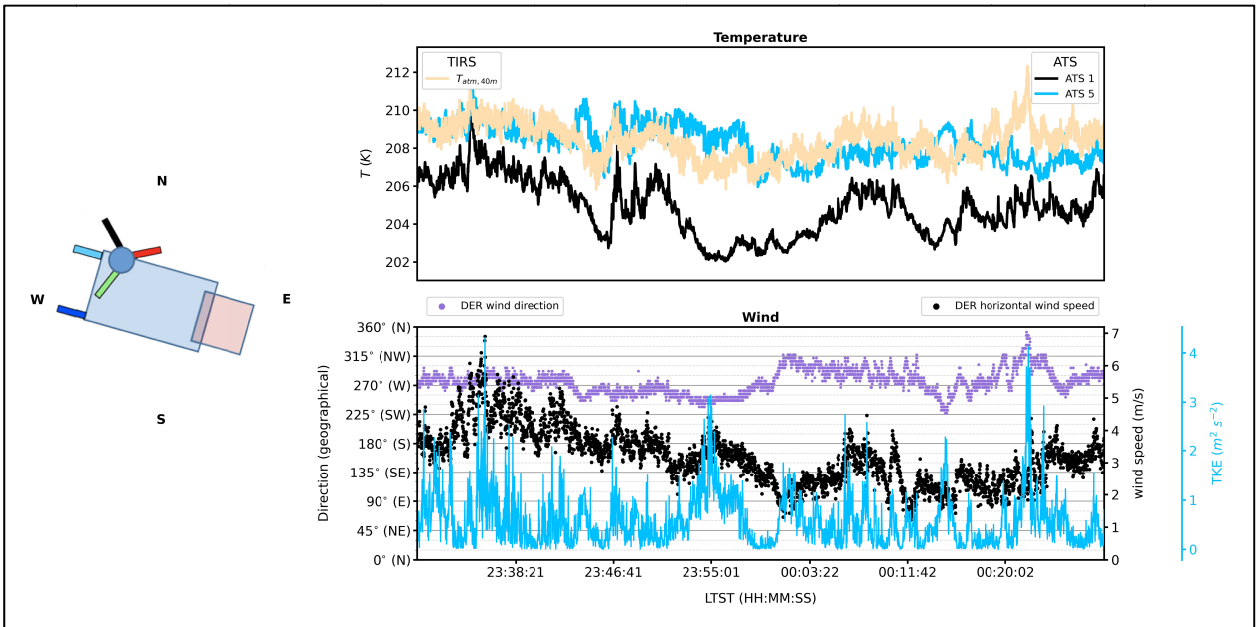


Figure S6. Same as Figure 3 but for sol 239 (*Ls* 116) from 23:30-00:30.

43
44
45

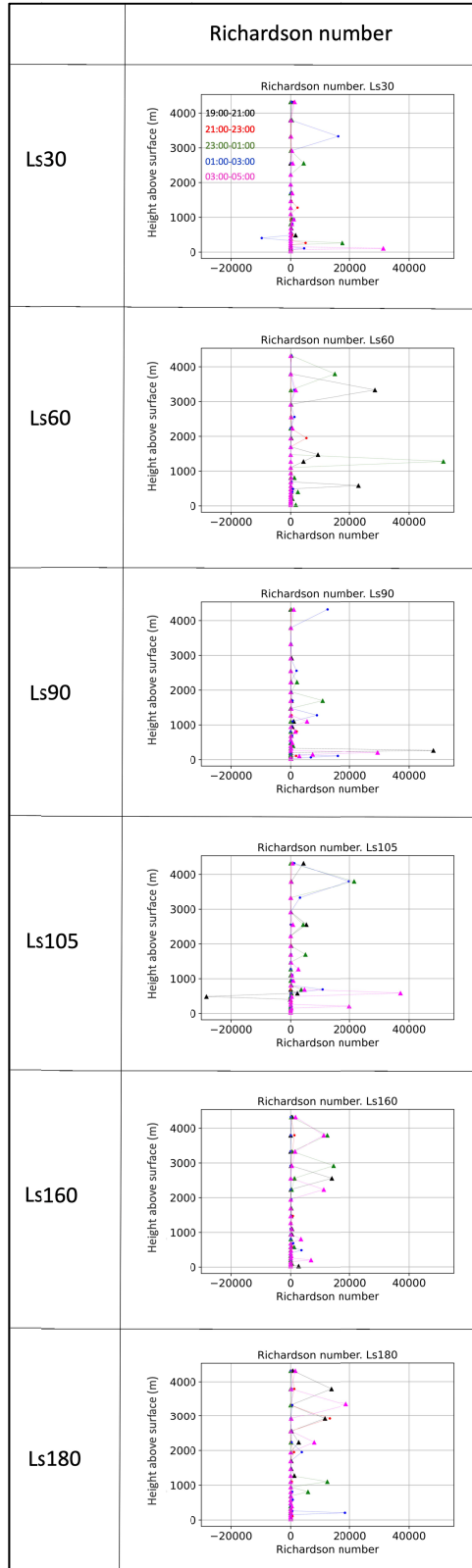


Figure S7. Same as Figure 14 but only for the whole range of Richardson number (Ri)

46
47
48
49